

Nanoscale

Accepted Manuscript



This is an *Accepted Manuscript*, which has been through the Royal Society of Chemistry peer review process and has been accepted for publication.

Accepted Manuscripts are published online shortly after acceptance, before technical editing, formatting and proof reading. Using this free service, authors can make their results available to the community, in citable form, before we publish the edited article. We will replace this *Accepted Manuscript* with the edited and formatted *Advance Article* as soon as it is available.

You can find more information about *Accepted Manuscripts* in the [Information for Authors](#).

Please note that technical editing may introduce minor changes to the text and/or graphics, which may alter content. The journal's standard [Terms & Conditions](#) and the [Ethical guidelines](#) still apply. In no event shall the Royal Society of Chemistry be held responsible for any errors or omissions in this *Accepted Manuscript* or any consequences arising from the use of any information it contains.

ARTICLE

The Novel Behaviours of Multiferroic Properties in Na Doped BiFeO₃ Nanoparticles

Cite this: DOI: 10.1039/x0xx00000x

Hong Zhang,^a Weifang Liu,^{*a} Ping Wu,^a Xiao Hai,^{ae} Minchen Guo,^a Xiaojuan Xi,^b Ju Gao,^c Xu Wang,^b Feng Guo,^b Xunling Xu,^a Can Wang,^d Guangyao Liu^d Weiguo Chu^e and Shouyu Wang^{*bc},

Received 00th January 2012,
Accepted 00th January 2012

DOI: 10.1039/x0xx00000x

www.rsc.org/

Highly aliovalent Na¹⁺ ions are selected as dopant to substitute Bi³⁺ ions of BiFeO₃ (BFO) and Bi_{1-x}Na_xFeO₃ (x=0, 0.01, 0.03, 0.05) nanoparticles are prepared via a facile sol-gel method. Weak ferromagnetism and obvious exchange bias phenomenon (EB) without field cooling are observed in the samples. To ascertain the presence of EB in the present nanoparticles, the training effect (TE) has been investigated and fitted by Binek's model. Moreover, with the increase of Na¹⁺ content, the band gap is decreased, while interestingly, the leakage current density is significantly reduced and the smallest leakage current density (~10⁻⁷ A cm⁻²) is observed for the 3% Na doped BFO. The electrical conduction mechanism of samples is investigated by plotting log *J* versus log *E*. Oxygen vacancies decrease with the increase of Na content analyzed through X-ray photoelectron spectroscopy (XPS) measurements. To further explain the decrease of band gap and leakage current density with the increase of Na content, the interplay of oxygen vacancies and holes is analyzed and a phenomenological qualitative model based on the electronic energy band is proposed.

1. Introduction

Multiferroic materials, including ferroelectricity and ferromagnetism (or antiferromagnetism) ordering in a single phase and even coupling magnetoelectricity between them, have attracted extensive studies due to their potential applications in information storage.¹⁻⁴ However, these kinds of materials are rare in ABO₃ type of perovskite materials, since for being simultaneously ferroelectric and ferromagnetic the material requires empty and partially filled transition metal d-orbitals, respectively, which are mutually exclusive properties.⁵ Among these rare ABO₃ type of perovskite multiferroic materials, from the practical application point of view, BiFeO₃ (BFO) is the most promising, due to its multiferroic behaviors at room temperature with relatively high ferroelectric Curie (T_C~1103 K for bulk BFO) and G-type antiferromagnetic Neel (T_N~643 K for bulk BFO) temperatures.⁶

In recently years, a lot of investigations about ferroelectricity and ferromagnetism properties of its ceramic and nanostructure materials have been reported.⁷⁻¹⁰ Unfortunately, some serious drawbacks of BFO associated with its electrical and multiferroic properties hinder its potential applications, therefore, several challenges remain to be addressed. These include (i) weak ferroelectric remanent polarization,⁶ (ii) high leakage current density,¹¹ (iii) poor ferroelectric reliability,¹² and (iv) inhomogeneous weak magnetization.¹³ Accordingly, numerous attempts have been devoted to overcoming these obstacles. Due to the size effect and the large ratio of surface to volume, BFO nanoparticles exhibit significant property differences as compared to its bulk

counterparts. For instance, when the nanoparticle size is less than the periodicity of spin helical ordering structure (62 nm),¹⁴ the size effect can disrupt the spin helical ordering structure, which leads to the significantly enhanced magnetization of BFO nanoparticles.¹⁵ In addition, recent extensive investigations have focused on substitution of rare-earth or alkaline earth elements at A-site, B-site or A-B-site of BiFeO₃.¹⁶⁻¹⁸ The substitution at A-site could produce an obvious effect on the lattice structure and an imbalance of the Bi 6s² lone pair.¹⁹ This affects the ferroelectric behaviors of BFO and moderately affects the magnetism. On the other hand, the substitution at the B-site would directly affect its magnetic behaviors based on the destruction of the spin cycloid or the exchange interaction between the host Fe³⁺ ion and the dopant ions.²⁰ However, a few investigations have been reported on alkali elements as dopant to substitute A or B-site of BFO. Recently, Shirolkar et al reported BFO nanoparticles via Li doping on Fe site and found that the BFO lattice undergoes a large structural distortion even at a low doping concentration, which could be attributed to the high aliovalency of Li compared to Fe. Also, an enhancement in the magnetic moment per Fe atom was observed. In addition, the bistable resistive switching attributed to the oxygen vacancy mediated filamentary conduction phenomenon has also been observed.²¹

In fact, it has been reported that the substitution of alkali element Na can effectively improve the physical properties in other ABO₃ type of perovskite materials, for instance, the piezoelectric properties of Na-modified KNbO₃ ceramics can be enhanced.²² In this paper, we selected Na¹⁺ ions as dopant to substitute Bi³⁺ ions of BFO and prepared Bi_{1-x}Na_xFeO₃ (x=0,

0.01, 0.03, 0.05) nanoparticles via a facile sol-gel method, according to the facts: (i) approximate radius of Na^{1+} (1.18 Å) ion and Bi^{3+} ion (1.17 Å),²³ (ii) Na^{1+} being highly aliovalent compared to Bi^{3+} ion. Detailed studies of structure, magnetic and electrical properties of the samples were investigated. Due to charge neutrality, the substitution of aliovalent elements like Ca^{2+} , Ba^{2+} , Sr^{2+} , Ni^{2+} etc.²⁴⁻²⁷ at trivalent Bi-site or Fe-site, can easily influence the number of hole or electron carriers and oxygen vacancies in BFO. These defects can play an important role in the leakage properties, because they produce the impurity band between the valance band and conduction band, which reduces the band gap. In the Na doped samples, the band gap is decreased with the increase of Na^{1+} content, while interestingly, the leakage current density of samples is significantly reduced and the smallest leakage current density ($\sim 10^{-7}$ A cm^{-2}) is observed in the 3% Na doped BFO. The simultaneous reduction in band gap and leakage current density is an uncommon behavior compared with other substitution at Bi-site of lower valent elements, such as Ca^{2+} , Ba^{2+} , Sr^{2+} etc.²⁴⁻²⁶ To explain this, the conduction mechanism of the present samples are investigated by plotting $\log J$ versus $\log E$. The interplay of oxygen vacancies and holes is analyzed and a phenomenological qualitative model is proposed based on the electronic energy band. Additionally, at room temperature, we have observed distinct exchange bias phenomenon (EB) without field cooling for Na doped BFO samples. To ascertain the presence of EB, we have studied training effect (TE) as well.

2. Experimental

$\text{Bi}_{1-x}\text{Na}_x\text{FeO}_3$ ($x=0, 0.01, 0.03, 0.05$) nanoparticles were synthesized by sol-gel method. High purity grade $\text{Bi}(\text{NO}_3)_3 \cdot 5\text{H}_2\text{O}$ and $\text{Fe}(\text{NO}_3)_3 \cdot 9\text{H}_2\text{O}$ in 1:1 molar ratio were mixed in analytical grade ethylene glycol to prepare precursor solution. Analytical grade tartaric acid was added to the solution in 1:1 molar ratio with respect to the precursors, and

the mixture was stirred continuously at 70 °C for 3 h. The solution was transparent, reddish-brown and clear sol. Then it was placed in a drying oven at 90 °C for 3 h until the clear sol was completely turned to yellowish-brown gel. The gel was further dried at 140 °C for 3 h, then annealed at 400 °C for 1.5 h, and finally ground into powders. Subsequently the powders were calcined for 2 h in air at 550 °C. The samples with different Na doping concentrations were synthesized by adding varying NaNO_3 content in the precursor solution and keeping all other experimental conditions constant.

The crystalline structure analysis of the samples was carried out by X-ray diffraction (XRD) (Rigaku D/MAX-2500 diffractometer with Cu K α radiation). The average particle size and microstructural properties of the samples were investigated by transmission electron microscopy (TEM), high resolution transmission electron microscopy (HRTEM) and the corresponding selected area electron diffraction (SAED) pattern using JEM-2100F instrument. The chemical states of the Fe ions were analyzed by X-ray photoelectron spectroscopy (XPS) which was recorded with PHI1600. Magnetic characterization of the samples was measured on Magnetic Property Measurement System (MPMS) SQUID-VSM made by Quantum Design. UV-vis absorption spectrum of our nanoparticle samples was performed by Shimadzu UV-3600 UV-VIS-NIR spectrophotometer. To study the electrical properties, the samples were pressed into pellets by compaction of powders in a uniaxial press, and the pellets were sintered for half an hour at 600 °C. The dielectric properties were measured by a precise impedance analyzer WK 6400 with an ac signal of 1000 mV. The leakage current curve was evaluated using an Axiacct model TF 2000 ferroelectric analyser. All the measurements were carried out at room temperature.

3. Results and discussion

X-ray diffraction and transmission electron microscopy

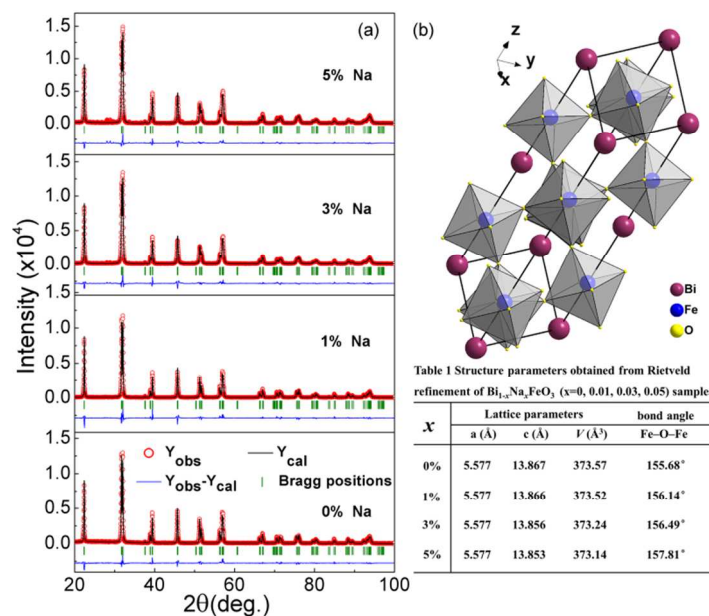


Fig. 1 (a) Rietveld refined XRD pattern of $\text{Bi}_{1-x}\text{Na}_x\text{FeO}_3$ ($x=0, 0.01, 0.03, 0.05$) nanoparticles at room temperature. The intensities were normalized for plotting. (b) The unit cell structure of BFO at normal conditions could be considered as distorted perovskite with strongly distorted FeO_6 octahedrons. Table 1 Structure parameters obtained from Rietveld refinement of samples.

The Rietveld refined XRD patterns of all the samples are shown in Fig. 1 (a), and it indicates that all the main XRD diffraction peaks can be well fitted with the rhombohedral distorted perovskite structure of BFO (space group: R3c). The detailed Refined structural parameters listed in Table S1 (Table S1 in the Supporting Information). Few minor impurity phase of $\text{Bi}_2\text{Fe}_4\text{O}_9$ appears in $\text{Bi}_{0.95}\text{Na}_{0.05}\text{FeO}_3$ sample. The unit cell structure of BFO considered as distorted perovskite with strongly distorted FeO_6 octahedrons at normal conditions is shown in Fig. 1 (b). The structural parameters obtained from the Rietveld refined XRD patterns for the pure and doped samples are given in Table 1. For the present pure BFO nanoparticles, the lattice parameters are little less than the value ($a=5.577\text{\AA}$, $c=13.867\text{\AA}$, $V=373.57\text{\AA}^3$) reported in literature, but the bond angle of Fe–O–Fe is slightly larger than that (155.68°) reported in literature.²⁸ For BFO, the octahedral tilt is about $11\text{--}14^\circ$ around the polar [111] axis, with the directly related Fe–O–Fe angle.³ As the Na doping concentration increases, the bond angle of Fe–O–Fe is also increased. This result illustrates that the FeO_6 octahedral tilting behavior is modulated in Na doped samples, and the similar result was also reported in Li doped BFO, Mn doped BFO and pure BFO nanoparticles.^{21, 29, 30}

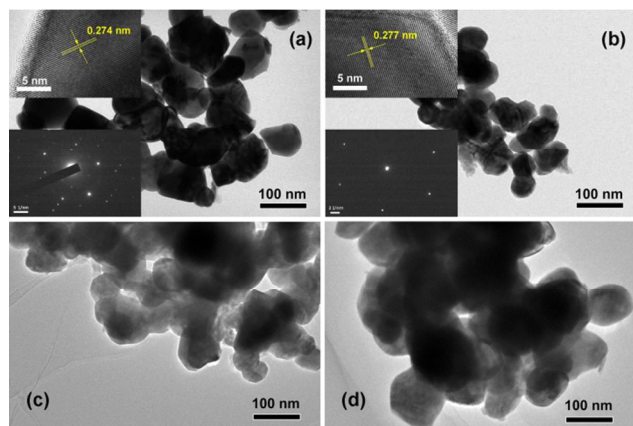


Fig. 2 TEM images of (a) undoped BFO nanoparticles, (b) 1% Na doped BFO nanoparticles, (c) 3% Na doped BFO and (d) 5% Na doped BFO nanoparticles. The selected area electron diffraction (SAED) pattern and the high resolution TEM (HRTEM) are shown in the upper and lower insets.

Fig. 2 shows TEM images of undoped and doped BFO nanoparticles. From the TEM images, it is observed that the shapes of most particles are nearly spherical but some of them are irregular and some agglomerations in nature are found. The average particle size obtained from TEM images for the undoped BFO sample is around 60 nm. For 1% and 3% Na doped sample, the average particle size is about 50 nm. While, for the 5% Na doped sample, there is no obvious change in the particle size compared with the undoped BFO sample. The selected area electron diffraction (SAED) pattern and the high resolution TEM (HRTEM) obtained from an individual BFO nanoparticle are shown in the upper and lower insets (Figure S1 in the Supporting Information for a larger view) of TEM image (a) and (b) respectively, which indicates the single-crystalline nature of our samples with a high degree of crystallinity.

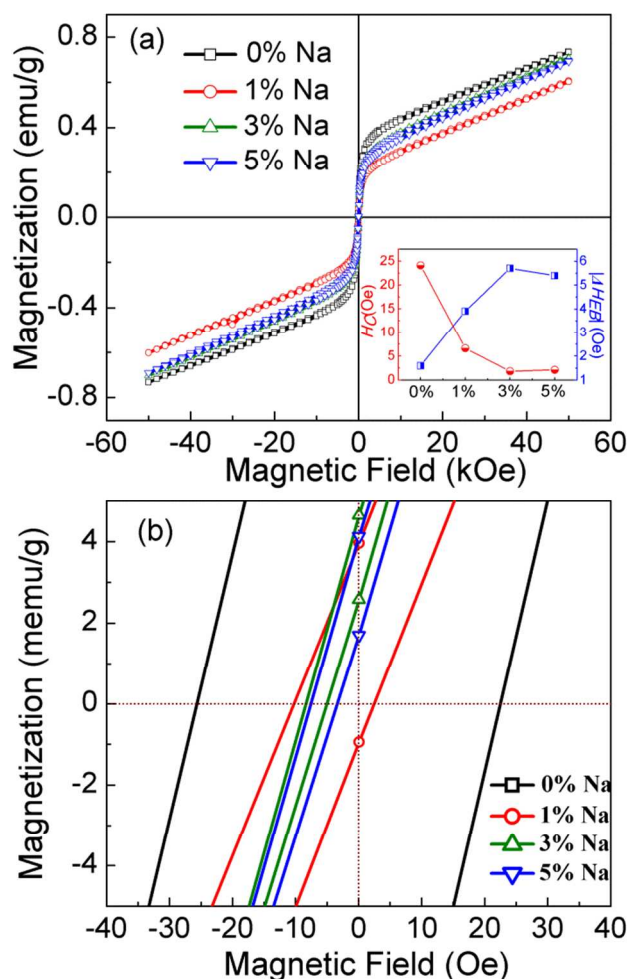


Fig. 3 (a) the field dependent magnetization hysteresis (M-H) loops of $\text{Bi}_{1-x}\text{Na}_x\text{FeO}_3$ ($x=0, 0.01, 0.03, 0.05$) nanoparticles at room temperature. (b) The enlargement of Fig. 3 (a) at magnetic field range from -40 Oe to $+40$ Oe.

Magnetization and exchange bias phenomenon

The field dependent magnetization hysteresis (M-H) loops of the samples at room temperature are shown in Fig. 3 (a). In contrast to the antiferromagnetism for bulk BFO, all our nanoparticle samples show weak ferromagnetism at room temperature, which is consistent with other reports of BFO nanoparticles.^{15, 31} In bulk BFO, the magnetization at room temperature is suppressed by the G-type antiferromagnetism ordering structure and a spin helical ordering structure with a periodicity of 62 nm. The G-type antiferromagnetism ordering structure can be described as comprising two spin sublattices with ferromagnetic interactions within one sublattice and antiferromagnetic interactions between sublattices.³ While in BFO nanoparticle system, the periodic spiral-modulated spin structure can be modified due to the reduction in the particle size. Meanwhile, the large ratio of surface to volume of nanoparticles can lead to the frequent interruption of long-range antiferromagnetic order and the magnetic uncompensation between two spin sublattices at the particle surfaces.¹⁵ In addition, with the increase content of dopant, the surface strain and the lattice distortion can give rise to the modulation of the local spin canting, with a net result that

uncompensated spins are produced.^{32, 33} Thus, the weak ferromagnetism of our nanoparticle samples can be primarily attributed to two aspects: one is the suppression of the spin helical ordering structure derived from the size effect; the other one is the contribution of uncompensated spins at the surface due to the large ratio of surface area to volume and the local spin canting.³⁴ Compared with undoped sample, the magnetization of Na doped samples is reduced, which is mainly due to the weakened magnetic interaction caused by the increase of Fe–O–Fe angle with increase of Na¹⁺ content. However, the magnetization of 3% Na doped sample is enhanced, which may be attributed to the contribution from minor impurity phase of antiferromagnetic Bi₂Fe₄O₉,³⁵ observed from zoomed view of XRD pattern. For 5% Na doped sample, the magnetization is nearly same with that of 3% Na doped sample, which may be due to the interplay of increased Bi₂Fe₄O₉ impurity phase and increased particle size.

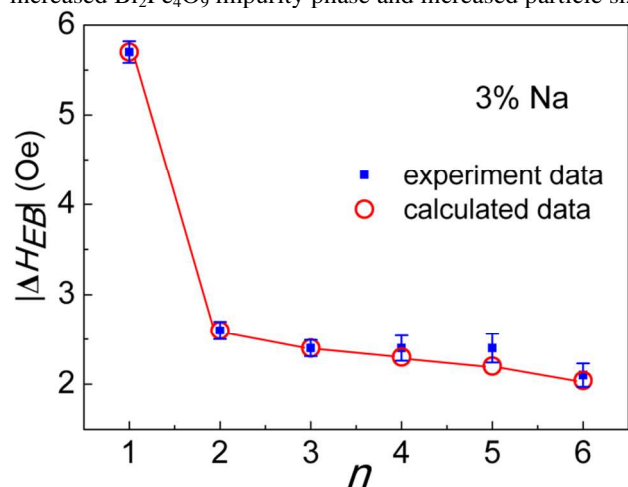


Fig. 4 The open circles are the experimental data points of the exchange bias field (ΔH_{EB}) dependence on the number of field cycles (n). The solid squares represent the calculated data points using Binek's recursive formula, and the solid line is a guide to eye.

Fig. 3 (b) shows the enlargement of Fig. 3 (a) at magnetic field range from -40 Oe to $+40$ Oe. Interestingly, without field cooling, the distinct shifted hysteresis loops are observed for Na doped BFO samples. This is expected to be interpreted as the presence of exchange bias phenomenon (EB). To ascertain the presence of EB in the present nanoparticles, we have studied the training effect (TE) shown in Fig. 4, which is considered to be an important characteristic of conventional EB systems.²⁹ For the 3% Na¹⁺ doped BFO nanoparticles, a monotonic decrease in exchange bias field (ΔH_{EB}) has been observed with the increase of field cycles number (n). The experimental data points were fitted by Binek's model³⁶ with a recursive formula for:

$$H_{EB}(n+1) - H_{EB}(n) = -\Gamma [H_{EB}(n) - H_{EB}(\infty)]^3 \quad (1)$$

where $H_{EB}(n)$ and $H_{EB}(\infty)$ are magnitudes of EB field for the n th cycle and for the limit of infinite loops, respectively, Γ is a system-dependent constant, and the fitted parameters are $H_{EB}(\infty) = 0.524$ T and $\Gamma = 0.022$. The experimentally observed TE data points are in accordance with Binek's model based on antiferromagnetic (AFM) and ferromagnetic (FM) interface. According to above described magnetic mechanism, in nanoparticle system, the uncompensated spins at the surface are ferromagnetic interactions, but the spins in the inner of nanoparticle are antiferromagnetic order, which can be

represented as an AFM core and FM shell in nature.²⁴ This demonstrates that the observed shift in hysteresis loop is EB phenomenon and it occurs due to an interface exchange coupling between the core and shell of the present Na doped BFO nanoparticle system.³⁷ From the inset of Fig. 3 (a), it can be found the exchange bias field (ΔH_{EB}) is increased and the coercivity (H_C) is decreased with the increase of Na¹⁺ ions content. The increase of ΔH_{EB} may be attributed to the enhancement of interface exchange interaction due to the modulation of the uncompensated spins at the surface by Na¹⁺ doping in the Bi-site. As reported, the thermal effects are more pronounced and important with the decrease of particle size for nanoparticle samples.³⁸ So the small coercivity of the samples could be attributed to the thermal effects.

Analysis of UV-vis absorption and leakage current density

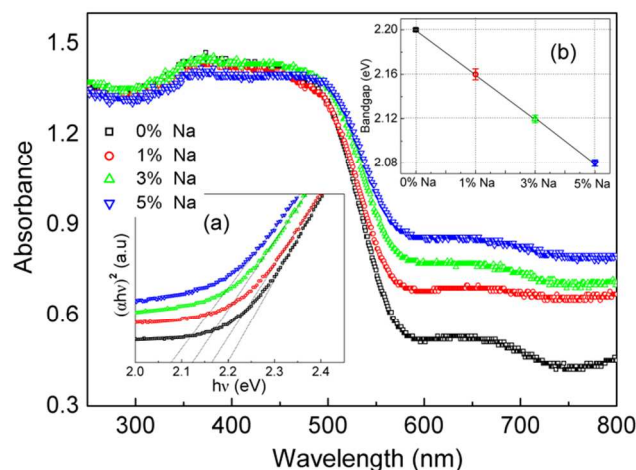


Fig. 5 UV-vis absorption spectrum of Bi_{1-x}Na_xFeO₃ ($x=0, 0.01, 0.03, 0.05$) nanoparticles. Inset (a): $(\alpha hv)^2$ versus hv plot of samples. Inset (b): the band gap estimated from lower inset is plotted as a function of x ($x=0, 0.01, 0.03, 0.05$).

In Fig. 5, the UV-vis absorption spectra of the Bi_{1-x}Na_xFeO₃ ($x=0, 0.01, 0.03, 0.05$) nanoparticles was measured at room temperature. In the rhombohedral, BFO should in practice behave as a direct-band gap semiconductor at room temperature.³ Band gap E_g for the direct band gap materials can be calculated by using the Tauc relation: $(\alpha hv)^2 = K(hv - E_g)$,³⁹ where K is a constant, α is the absorption coefficient and hv is the photon energy. The plots of $(\alpha hv)^2$ versus hv for Bi_{1-x}Na_xFeO₃ samples with $x=0, 0.01, 0.03, 0.05$ and the value of the band gap estimated by the linear extrapolation approach are shown in inset (a) and (b) of Fig. 5, respectively. The band gap of undoped BFO nanoparticles is estimated to be 2.2 eV which is in accordance with the earlier reported band gap values.⁴⁰ While, with the increase content of Na¹⁺ ions, the band gap is clearly reduced (2.16 eV, 2.12 eV, 2.08 eV for 1%, 3%, 5% Na doped samples respectively). This can be explained by two aspects. On the one hand, it can be observed in Table 1 that the angle of Fe–O–Fe is increased with the increase of Na¹⁺ content. According to the report of Borisevich et al.,⁴¹ the increase of the Fe–O–Fe angle (towards 180°) increases the bandwidth of occupied and unoccupied bands by directly changing the electronic structure of the central cation and the interfacial electronic property, which can reduce the band gap of the Na doped BFO samples. The

other important reason is the existence of impurity-induced energy levels inside the forbidden gap region, for instance oxygen vacancy, hole and so on, and the impurities band can lead to the decrease of band gap.⁴² Meanwhile, these impurity defects play a key role in electrical transport property.

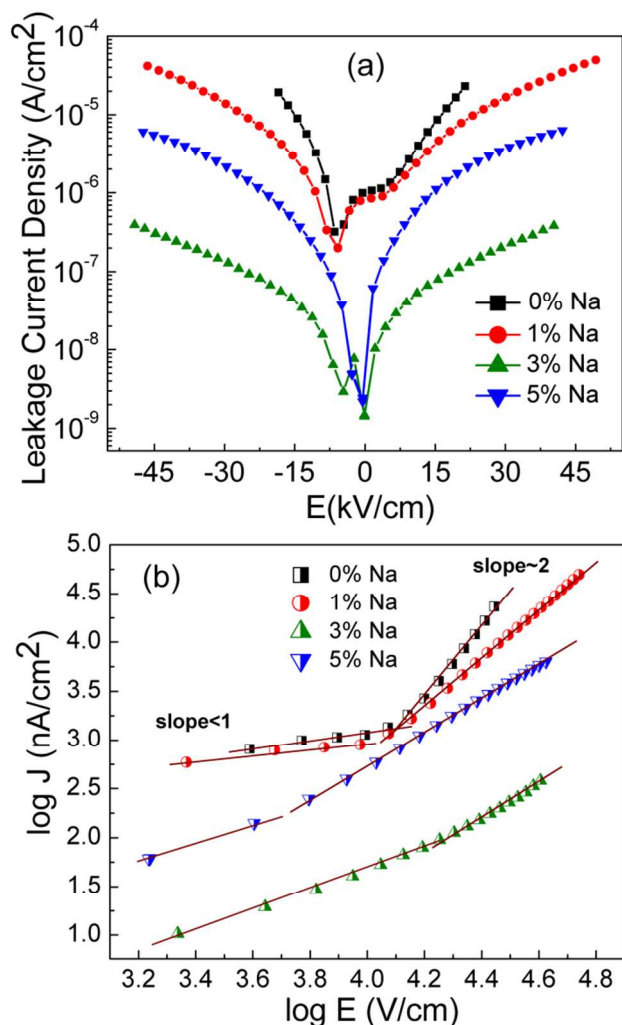


Fig. 6 (a) Leakage current as a function of applied electric field (J - E) and (b) $\log(J)$ versus $\log(E)$ plot for the samples for $\text{Bi}_{1-x}\text{Na}_x\text{FeO}_3$ ($x=0, 0.01, 0.03, 0.05$) nanoparticles at room temperature.

Fig. 6 (a) shows the leakage current density (J) as a function of applied electric field (E) for the $\text{Bi}_{1-x}\text{Na}_x\text{FeO}_3$ ($x=0, 0.01, 0.03$) samples. Interestingly, with the increase of Na^{1+} content, the leakage current of the samples is significantly reduced and the smallest leakage current density ($\sim 10^{-7}$ A cm^{-2}) is observed in the 3% Na doped BFO sample. To get further insight into the leakage behavior, the electrical conduction mechanism of the present samples is investigated by plotting $\log J$ versus $\log E$ as shown in Fig. 6 (b). According to the power law $J \propto E^m$ relationship, the different values of slope 'm' of these curves give the information about the different conduction mechanism. At relatively lower electric fields ($\log E = 3.5$ - 4.1 V cm^{-1} for undoped BFO), the $\log J$ vs $\log E$ plot is linear and the slope is close to 1, which represents that the leakage currents show Ohmic behavior originated from the thermal emission of electrons. In the high

electric field range ($\log E = 4.1$ - 4.5 V cm^{-1} for undoped BFO), the slope is close to 2, which agrees well with the space charge limited conduction (SCLC) mechanism. The SCLC is considered as a normal leakage behavior and correlates with oxygen vacancies in BFO materials.⁴³ From Fig. 6 (b), it can be seen that with the increase of Na^{1+} ions content, the slope in low electric field is gradually increased, but it is obviously decreased in the high electric field. Meanwhile, the electric field range of the slope ~ 1 gradually extends from $\log E = 3.5$ - 4.1 V cm^{-1} for undoped BFO to $\log E = 3.2$ - 4.3 V cm^{-1} for 3% doped BFO, and it decreases for the slope ~ 2 from $\log E = 4.1$ - 4.5 V cm^{-1} for undoped BFO to $\log E = 4.3$ - 4.6 V cm^{-1} for 3% doped BFO. This indicates that the SCLC correlated with oxygen vacancies is dominant for undoped BFO sample, while in Na doped BFO samples, the Ohmic behavior originated from the thermal emission of electrons is enhanced and the SCLC of the samples get more and more weak with the increase of Na^{1+} ions content, which indicates that the amount of oxygen vacancies is decreased.

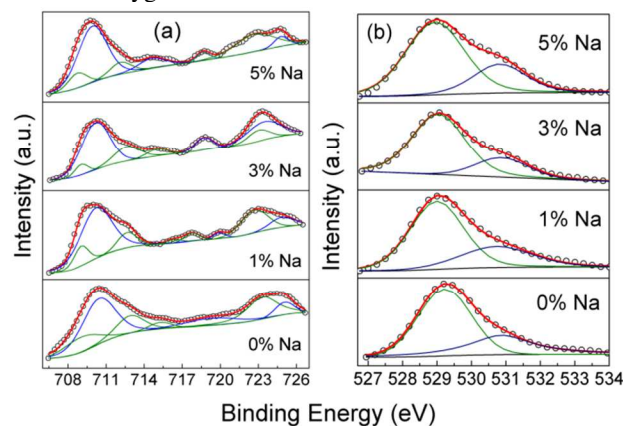


Fig. 7 XPS spectra of (a) the Fe2p lines and (b) the O1s for $\text{Bi}_{1-x}\text{Na}_x\text{FeO}_3$ ($x=0, 0.01, 0.03, 0.05$) nanoparticles.

To further elucidate the variation of oxygen vacancies in the samples with different Na content, the XPS measurements were carried out. Fig. 7 (a) and (b) show the XPS spectra analysis of the Fe2p and O1s core level regions, respectively, by Lorentzian-Gaussian fitting for $\text{Bi}_{1-x}\text{Na}_x\text{FeO}_3$ ($x=0, 0.01, 0.03$) samples, where the core level binding energies were aligned with respect to C1s peak (284 eV). Due to different d orbital electron configurations caused by relaxation of the metal ions, Fe^{2+} and Fe^{3+} always show the satellite peak at 6 eV or 8 eV above their $2p_{3/2}$ principal peaks, respectively, which were reported to be characteristic of the oxidation states of the Fe.⁴⁴ By fitting the peaks for the valence states of Fe ions, the results reveal that the Fe^{3+} oxidation state coexists with Fe^{2+} oxidation state in all samples and the binding energy peak position of Fe $2p_{3/2}$ is located about at 709.5 eV for Fe^{2+} (olive line) and 710.4 eV for Fe^{3+} (blue line). According to the fitting, the ratio of $\text{Fe}^{3+}:\text{Fe}^{2+}$ is calculated to be 16:5 ($x=0$), 28:5 ($x=0.01$), 50:5 ($x=0.03$) and 32:5 ($x=0.05$) for $\text{Bi}_{1-x}\text{Na}_x\text{FeO}_3$. In Fig. 7 (b), the asymmetric O1s spectra were fitted and the left peak (olive line) in binding energy located at about 529.5 eV is attributed to the intrinsic O^{2-} ions in the samples; the right one (navy line) located at about 531 eV is ascribed to the O^{2-} ions located in the oxygen vacancies deficient regions. With the increase of Na^{1+} ions content at Bi-site, the content of Fe^{3+} is increased and the amount of oxygen vacancies is decreased. The maximum ratio of $\text{Fe}^{3+}:\text{Fe}^{2+}$ and

the least content of oxygen vacancies can be observed in 3% Na doped sample from the Fig. 7 (a) and (b). Therefore, with the increase of the Na^{1+} ions content, the decrease of leakage

current density is attributed to the increase of Fe^{3+} and the decrease of oxygen vacancies.

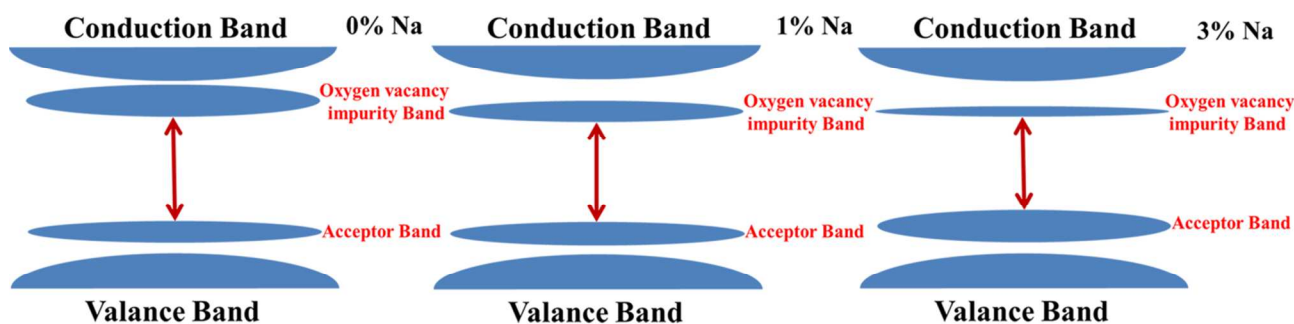
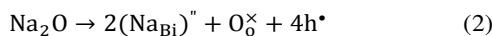
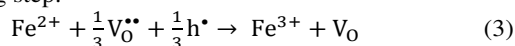


Fig. 8 A schematic diagram of the possible mechanism for electronic energy band.

In lower-valence elements than $\text{Bi}^{3+}/\text{Fe}^{3+}$ doped BFO systems, the increased defects (oxygen vacancies) play an important role in reduction of band gap, and simultaneously significantly influence the leakage properties. In the $\text{Bi}_{1-x}\text{Ca}_x\text{FeO}_{3-\delta}$ films reported by Yang et al.,²⁴ an electronic conductor–insulator transition by control of band-filling was presented and discussed on the basis of the oxygen vacancies. Vagadia et al. reported an improved resistive switching effect in Ba-doped BiFeO_3 films, which was explained by the oxygen vacancy migration and recombination under positive and negative bias.⁴⁵ Recently, in Li^{1+} doped BFO nanoparticles reported by Shirolkar et al, the bistable resistive switching attributed to the oxygen vacancy mediated filamentary conduction phenomenon also has been observed.²¹ While interestingly, in our samples, the band gap is reduced, meanwhile, the leakage current density of samples also is significantly decreased. This is obviously different with the other lower valent elements doped BFO systems. To better understand the decrease of leakage current density and meanwhile the decrease of band gap with increasing of Na^{1+} ions content, a phenomenological qualitative model is proposed. A schematic diagram of the possible mechanism for electronic energy band is shown in Fig. 8. At per Na^{1+} substituted Bi^{3+} -site, there are two valence electrons deficient to coordinate with contiguous oxygen. Thus, the holes (h^*) are produced in this process. The main process can be described as follows:



In Fig. 8, the hole as an acceptor band locates the top of valance band and the oxygen vacancy impurity band locates at the bottom of conduction band as a kind of donor level. The increased concentration of holes produced by substitution of Na^{1+} at Bi-site gives rise to the wider acceptor band, so the band gap is decreased with the increasing of Na^{1+} content. At meanwhile, the increased holes need the electrons to recombine in nature, and the electrons could be provided by Fe^{2+} . This can promote the transformation from Fe^{2+} to Fe^{3+} and the consumption of oxygen vacancies, which can be supported by the experiment data from XPS, as illustrated by the following step:



As a consequence of ionization, the oxygen vacancies are mobile positive charges and can move through the sample under electric fields to find a new thermodynamic equilibrium,²⁴ which is a main factor for the large leakage

current density in undoped BFO nanoparticles. With the increase of Na^{1+} ions content, the consumption of oxygen vacancies makes the SCLC in the samples weaker and weaker, which gives rise to the decreased leakage current density. In addition, with the increase of Na^{1+} content, the broaden acceptor band at the top of valance band is helpful for the jump of thermal emission electrons at relatively lower electric fields, which is in accordance with enhancement of Ohmic behavior. This can be proved in the plot of $\log J$ vs $\log E$ in electric fields region of slope ~ 1 . However, the holes impurity band is deep acceptor level, compared with oxygen vacancies, so the contribution of the thermal emission electrons to the leakage current density of the samples is small. Thus the decrease of band gap and leakage current density with the increase of Na^{1+} content can be explained by the broaden hole acceptor band and the decrease of oxygen vacancies.

Dielectric properties

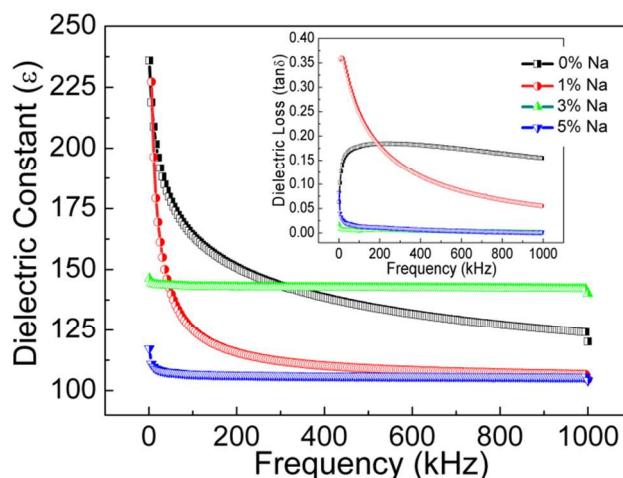


Fig. 9 The dielectric constant of $\text{Bi}_{1-x}\text{Na}_x\text{FeO}_3$ ($x=0, 0.01, 0.03, 0.05$) nanoparticles at room temperature. The inset shows the dielectric loss of all samples.

Fig. 9 and the inset show the frequency dependence of dielectric constant and dielectric loss of the $\text{Bi}_{1-x}\text{Na}_x\text{FeO}_3$ ($x=0, 0.01, 0.03$) samples, respectively. The dielectric constant of undoped and 1% Na doped BFO samples is decreased drastically with the increase of frequency in low frequency

region, called the f -sensitive region, and then tends to be constant when the frequency reaches a certain value (the f -stable region). This phenomenon can be attributed to the combined response of the orientational relaxation of dipoles and the conduction of charge carriers. Such behavior can be well described by the Maxwell-Wagner model,^{46, 47} which is related to the space charge relaxation at the interface. These space charges (e.g. oxygen vacancies and bismuth vacancies) can follow the applied electric field at low frequencies range (f -sensitive region) and contribute to the dielectric constant. At higher frequencies (the f -stable region), they do not have time to follow the applied field and undergo relaxation due to their large effective masses compared with dipoles.⁴⁸ While in 3% Na doped sample, the dielectric constant is stable in all frequency region. This indicates the content of the oxygen vacancies is reduced, which is in accordance with the above observations. A decrease in dielectric loss has been observed in the inset of Fig. 9 with the increase of Na concentration and when the concentrations of Na are 3% and 5%, the dielectric loss is the least

4. Conclusion

Undoped and Na doped BFO nanoparticles have been successfully synthesized through a modified sol-gel methods. Through M-H measurements, it is observed that nanoparticles show a weak ferromagnetic nature, which is attributed to the suppression of the spin helical ordering structure and the contribution of uncompensated spins at the surface. A distinct exchange bias phenomenon (EB) is observed without field cooling for Na doped BFO samples, which can be attributed to the core (AFM)-shell (FM) structure. Additionally, with the increase of Na content, the band gap and the leakage current of samples is significantly reduced and the smallest leakage current density ($\sim 10^{-7}$ A cm⁻²) are observed for the 3% Na doped BFO. The conduction mechanism of the present samples is investigated by plotting $\log J$ versus $\log E$. The Ohmic behavior originated from the thermal emission of electrons is enhanced and the SCLC correlated with oxygen vacancies of the samples get more and more weak with the increase of Na¹⁺ ions content. Based on the electronic energy band, a phenomenological qualitative model is proposed. The decrease of band gap and leakage current density can be explained by the broaden hole acceptor band and the decrease of oxygen vacancies. The dielectric constant is stable with the increase of frequency and the dielectric loss is the least for 3% and 5% Na doped BFO nanoparticles.

Acknowledgements

This work was funded by the Research Grant Council of Hong Kong (Project No. HKU 702112P and RGC 701813), the National Natural Science Foundation of China (11004148, 11104202).

Notes and references

^a Tianjin Key Laboratory of Low Dimensional Materials Physics and Preparing Technology, Faculty of Science, Tianjin University, Tianjin 300072, P. R. China.

^b College of Physics and Material Science, Tianjin Normal University,

Tianjin 300074, P. R. China.

^c Department of Physics, the University of Hong Kong, Pokfulam Road, Hong Kong.

^d Beijing National Laboratory for Condensed Matter Physics, Institute of Physics, Chinese Academy of Sciences, Beijing 100190, P. R. China.

^e National Center For Nanoscience and Technology of China, Beijing 100190, P. R. China.

- H. Schmid, *Ferroelectrics*, 1994, **162**, 19.
- N. A. Hill, *J. Phys. Chem. B*, 2000, **104**, 6694.
- G. Catalan, J. F. Scott, *Adv. Mater.*, 2009, **21**, 2463.
- J. F. Scott, *J. Mater. Chem.*, 2012, **22**, 4567.
- W. Eerenstein, N. D. Mathur and J. F. Scott, *Nature*, 2006, **442**, 759.
- J. Wang, J. B. Neaton, H. Zheng, V. Nagarajan, S. B. Ogale, B. Liu, D. Viehland, V. Vaithyanathan, D. G. Schlom, U. V. Waghmare, N. A. Spaldin, K. M. Rabe, M. Wuttig and R. Ramesh, *Science*, 2003, **299**, 1719.
- S. Karimi, I. M. Reaney, I. Levin and I. Sterianou, *Appl. Phys. Lett.*, 2009, **94**, 112903.
- P. Chen, X. Xu, C. Koenigsmann, A. C. Santulli, S. S. Wong and J. L. Musfeldt, *Nano Letters*, 2010, **10**, 4526.
- A. Q. Jiang, C. Wang, K. J. Jin, X. B. Liu, J. F. Scott, C. S. Hwang, T. A. Tang, H. B. Lu and G. Z. Yang, *Adv. Mater.*, 2011, **23**, 1277.
- S. Hong, T. Choi, J. H. Jeon, Y. Kim, H. Lee, H.Y. Joo, I. Hwang, J. S. Kim, S. O. Kang, S. V. Kalinin and B. H. Park, *Adv. Mater.*, 2013, **25**, 2339.
- X. Qi, J. Dho, R. Tomov, M. G. Blamire and J. L. MacManus-Driscoll, *Appl. Phys. Lett.* 2005, **86**, 062903.
- S. Y. Yang, F. Zavaliche, L. Mohaddes-Ardabili, V. Vaithyanathan, D. G. Schlom, Y. J. Lee, Y. H. Chu, M. P. Cruz, Q. Zhan, T. Zhao and R. Ramesh, *Appl. Phys. Lett.*, 2005, **87**, 102903.
- B. Ruetter, S. Zvyagin, A. P. Pyatakov, A. Bush, J. F. Li, V. I. Belotelov, A. K. Zvezdin and D. Viehland, *Phys. Rev. B*, 2004, **69**, 064114.
- D. Lebeugle, D. Colson, A. Forget, M. Viret, A. M. Bataille and A. Gukasov, *Phys. Rev. Lett.*, 2008, **100**, 227602.
- T. J. Park, G. C. Papaefthymiou, A. J. Viescas, A. R. Moodenbaugh and S. S. Wong, *Nano Letters*, 2007, **7**, 766.
- G. S. Lotey, N. K. Verma, *J. Nanopart. Res.*, 2012, **14**, 742.
- D. P. Dutta, B. P. Mandal, R. Naik, G. Lawes and A. K. Tyagi, *J. Phys. Chem. C*, 2013, **117**, 2382.
- K. Chakrabarti, K. Das, B. Sarkar, S. Ghosh, S. K. De, G. Sinha and J. Lahtinen, *Appl. Phys. Lett.*, 2012, **101**, 042401.
- J. Bielecki, P. Svedlindh, D. T. Tibebe, S. Cai, S. G. Eriksson, L. Borjesson and C. S. Knee, *Phys. Rev. B*, 2012, **86**, 184422.
- C. H. Yang, D. Kan, I. Takeuchi, V. Nagarajan and J. Seidel, *Phys. Chem. Chem. Phys.*, 2012, **14**, 15953.
- M. M. Shirolkar, C. Hao, X. Dong, T. Guo, L. Zhang, M. Li and H. Wang, *Nanoscale*, 2014, **6**, 4735.
- H. L. Du, W. C. Zhou, F. Luo, D. M. Zhu, S. B. Qu and Z. B. Pei, *Appl. Phys. Lett.*, 2007, **91**, 202907.
- R. D. Shannon, *Acta Crystallogr.*, 1976, **A32**, 751.
- C. H. Yang, J. Seidel, S. Y. Kim, P. B. Rossen, P. Yu, M. Gajek, Y. H. Chu, L. W. Martin, M. B. Holcomb, Q. He, P. Maksymovych,

- N. Balke S. V. Kalinin, A. P. Baddorf, S. R. Basu, M. L. Scullin and R. Ramesh, *Nature Materials*, 2009, **8**, 485.
- 25 D. H. Wang, W. C. Goh, M. Ning and C. K. Ong, *Appl. Phys. Lett.*, 2006, **88**, 212907.
- 26 V. A. Khomchenko, D. A. Kiselev, J. M. Vieira, A. L. Kholkin, M. A. Sá and Y. G. Pogorelov, *Appl. Phys. Lett.*, 2007, **90**, 242901.
- 27 X. D. Qi, J. Dho, R. Tomov, M. G. Blamire and J. L. MacManus-Driscoll, *Appl. Phys. Lett.* 2005, **86**, 062903.
- 28 F. Kubel, H. Schmid, *Acta Cryst.*, B 1990, **46**, 698.
- 29 P. K. Manna, S. M. Yusuf, R. Shukla, A. K. Tyagi. *Phys. Rev. B*, 2011, **83**, 184412.
- 30 F. Z. Huang, X. L. Wang, J. Zhang, K. Min, W. Lin, R. Ti, T. Xu, J. He, C. Yue and J. Zhu, *Sci. Rep.*, 2013, **3**, 2907.
- 31 W. W. Hu, Y. Chen, H. M. Yuan, G. H. Li, Y. Qiao, Y. Y. Qin and S. H. Feng, *J. Phys. Chem. C*, 2011, **115**, 8869.
- 32 C. Ederer, N. A. Spaldin, *Phys. Rev. B*, 2005, **71**, 060401.
- 33 M. Ramazanoglu, M. Laver, W. Ratcliff, II, S. M. Watson, W. C. Chen, A. Jackson, K. Kothapalli, Seongsu Lee, S. W. Cheong and V. Kiryukhin *Phys. Rev. Lett.*, 2011, **107**, 207206.
- 34 J. T. Richardson, D. I. Yiagas, B. Turk, K. Forster and M. V. Twigg, *J. Appl. Phys.*, 1991, **70**, 6977.
- 35 Z. M. Tian, S. L. Yuan, X. L. Wang, X. F. Zheng, S. Y. Yin, C. H. Wang and L. Liu, *J. Appl. Phys.*, 2009, **106**, 103912.
- 36 C. Binek, *Phys. Rev. B*, 2004, **70**, 014421.
- 37 S. Dong, K. Yamauchi, S. Yunoki, R. Yu, S. Liang, A. Moreo, J. M. Liu, S. Picozzi, E. Dagotto, *Phys. Rev. Lett.*, 2009, **103**, 127201.
- 38 B. D. Cullity, C. D. Graham, *Introduction to magnetic materials*, 2nd edn., Wiley, Piscataway, NJ, USA 2009, pp 361.
- 39 J. Tauc, *Amorphous and Liquid Semiconductors*, Plenum, New York, USA 1974.
- 40 U. A. Joshi, J. S. Jang, P. H. Borse and J. S. Lee, *Appl. Phys. Lett.*, 2008, **92**, 242106.
- 41 A.Y. Borisevich, H. J. Chang, M. Huijben, M. P. Oxley, S. Okamoto, M. K. Nranjan, J. D. Burton, E. Y. Tsymlal, Y. H. Chu, P. Yu, R. Ramesh, S. V. Kalinin and S. J. Pennycook, *Phys. Rev. Lett.*, 2010, **105**, 087204.
- 42 S. V. Pavana, C. Mocherla, R. Karthik, M. S. Ubic, R. Ramachandra and C. Sudakar, *Appl. Phys. Lett.*, 2013, **103**, 022910.
- 43 H. Yang, H. Wang, G. F. Zou, M. Jain, N. A. Suvorova, D. M. Feldmann, P. C. Dowden, R. F. DePaula, J. L. MacManus-Driscoll, A. J. Taylor and Q. X. Jia, *Appl. Phys. Lett.*, 2008, **93**, 142904.
- 44 L. Bi, A. R. Taussig, H. S. Kim, L. Wang, G. F. Dionne, D. Bono, K. Persson, G. Ceder and C. A. Ross, *Phys. Rev. B.*, 2008, **78**, 104106.
- 45 M. Vagadia, A. Ravalia, P. S. Solanki, R. J. Choudhary, D. M. Phase and D. G. Kuberkar, *Appl. Phys. Lett.*, 2013, **103**, 033504.
- 46 J. C. Maxwell, *Electricity and Magnetism*, Oxford University Press, Oxford, England, 1929, Vol. 1, Sec. 328.
- 47 K. W. Wagner, *Ann. Phys.*, 1913, **40**, 817.
- 48 Rectu, A. Agarwal, S. Sanghi and Ashima, *J. Appl. Phys.* 2011, **110**, 073909.